Journal Pre-proof

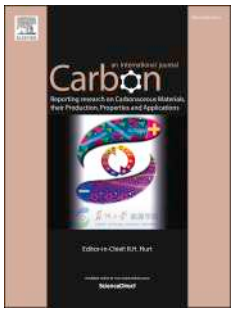

Lightweight carbon nanotube/aramid nanofiber aerogel with superior electromagnetic wave absorption, thermal insulation, and flame resistance

Anping Wang, Zhichun Zhang, Yanju Liu, Zibo Li, Jinsong Leng

PII: S0008-6223(24)00324-5

DOI: https://doi.org/10.1016/j.carbon.2024.119105

Reference: CARBON 119105

To appear in: *Carbon*

Received Date: 6 March 2024

Revised Date: 31 March 2024

Accepted Date: 4 April 2024

Please cite this article as: A. Wang, Z. Zhang, Y. Liu, Z. Li, J. Leng, Lightweight carbon nanotube/ aramid nanofiber aerogel with superior electromagnetic wave absorption, thermal insulation, and flame resistance, *Carbon* (2024), doi: https://doi.org/10.1016/j.carbon.2024.119105.

For Graphical Abstract

Lightweight carbon nanotube/aramid nanofiber aerogel with superior electromagnetic wave absorption, thermal insulation, and flame resistance

Anping Wang [a], Zhichun Zhang [a,*], Yanju Liu [b], Zibo Li [a], Jinsong Leng [a,*]

[a] *Centre for Composite Materials and Structures, Harbin Institute of Technology (HIT), Harbin 150080, People's Republic of China*

[b] *Department of Astronautic Science and Mechanics, Harbin Institute of Technology (HIT), Harbin 150001, People's Republic of China*

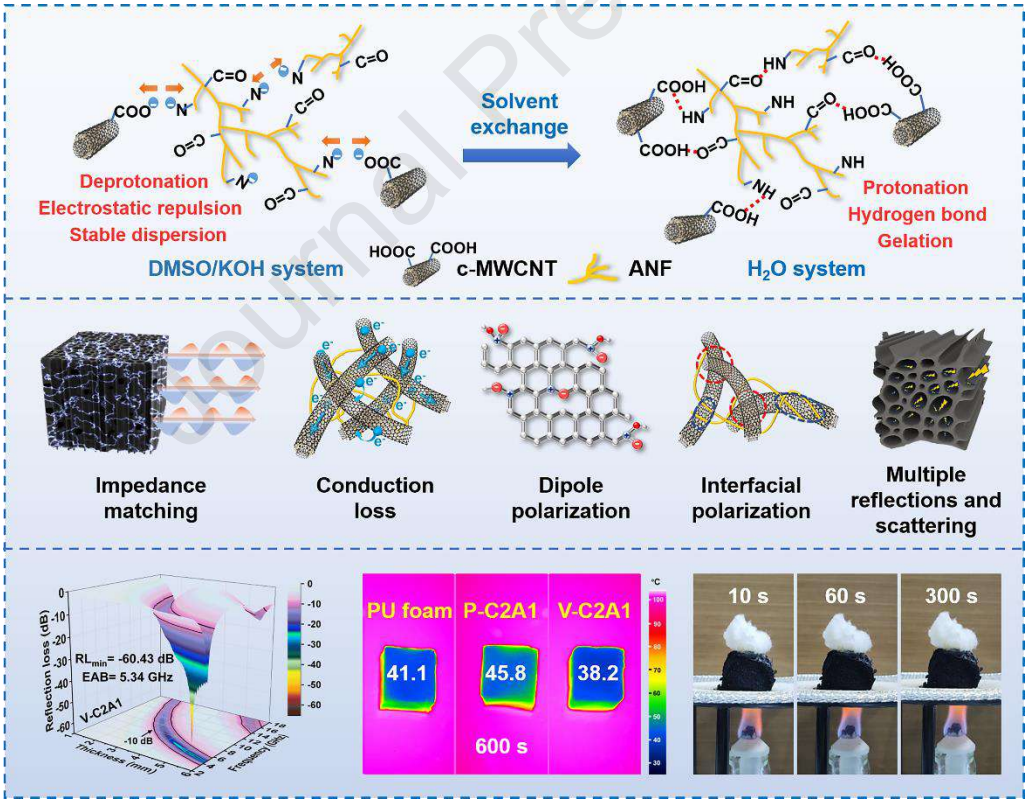

* Corresponding author. E-mail address: zczhang@hit.edu.cn (Z. Zhang)

* Corresponding author. E-mail address: lengjs@hit.edu.cn (J. Leng)

Lightweight carbon nanotube/aramid nanofiber aerogel with superior electromagnetic wave absorption, thermal insulation, and flame resistance

Anping Wang [a], Zhichun Zhang [a,*], Yanju Liu [b], Zibo Li [a], Jinsong Leng [a,*]

[a] *Centre for Composite Materials and Structures, Harbin Institute of Technology (HIT), Harbin 150080, People's Republic of China*

[b] *Department of Astronautic Science and Mechanics, Harbin Institute of Technology (HIT), Harbin 150001, People's Republic of China*

Abstract:

Carbon nanotubes, presenting distinguished electromagnetic wave (EMW) loss capacity and light-weight advantage, are promising candidates for EMW absorption materials. However, poor dispersibility, inadequate processibility, and excessive permittivity leading to impedance mismatch limit the application of carbon nanotubes. Herein, branched aramid nanofiber (ANF) acting as a surfactant, gelling agent, and electromagnetic parameter regulator is utilized to ameliorate the performances of carboxylic multi-walled carbon nanotube (c-MWCNT). The c-MWCNT/ANF aerogels with anisotropic structures are assembled through electrostatic-repulsion-assisted dispersion, hydrogen-bond-induced gelation, unidirectional freezing, and

* Corresponding author. E-mail address: zczhang@hit.edu.cn (Z. Zhang)

* Corresponding author. E-mail address: lengjs@hit.edu.cn (J. Leng)

freeze-drying. By adjusting the proportion of c-MWCNT and ANF to optimize the impedance matching and electromagnetic parameters, the composite aerogel with ultralow density (~ 26.2 mg cm^{-3}) shows an extraordinary minimum reflection loss of -60.43 dB and a maximum effective absorption bandwidth of 5.34 GHz along the vertical direction of oriented channels. Moreover, benefiting from high porosity and remarkable thermal stability, the aerogels possess prominent thermal insulation and flame resistance. This work provides a strategy for the advanced EMW absorption materials, which have great potential value for aerospace applications under harsh environments.

Keywords: aramid nanofiber, carboxylic multi-walled carbon nanotube, anisotropic aerogel, electromagnetic wave absorption, thermal insulation, flame resistance

1. Introduction

Mobile communication technology based on electromagnetic waves (EMW) has unprecedentedly realized real-time global connectivity, location, navigation, and remote control [1, 2]. Furthermore, EMW plays a crucial role in medical devices and home appliances [3]. However, the consequent electromagnetic pollution and radiation also inevitably pose a potential threat to human health, information security, and national defense security [4-6]. Electromagnetic wave absorption (EMWA) materials, capable of effectively converting electromagnetic energy into thermal energy, are qualified to mitigate these hazards [7]. The prevalent EMWA materials include magnetic metal/metallic oxide, conductive polymers, ceramics, and carbon materials [8-10]. Among them, carbon nanotube (CNT) has low density,

remarkable chemical durability, large specific surface area, and strong EMW loss capability, making CNT a distinguished candidate for EMWA materials [11].

Nevertheless, CNT as EMWA materials still face tremendous challenges in impedance matching due to excessive dielectric constant [12]. According to the academic viewpoint of dielectric "genes" proposed by Cao's group, the key to ameliorating the impedance matching and electromagnetic parameters of CNT is to tailor the conduction "genes" and polarization "genes" [13]. Currently, a variety of methods have been proven to be feasible to edit the "genes" [14, 15]. The first method involves modifying defects on CNT (*e.g.,* intrinsic defects, impurity defects, and interfaces) [16]. On the one hand, these defects enable the favorable design of the interaction between adjacent building units in nanomaterials [17]. On the other hand, the doped atoms can enhance the polarization "genes" of CNT [18, 19]. For instance, Chen et al. built N-doped CNT/carbon hollow spheres with a minimum reflection loss (RL_{min}) of -64.75 dB and an effective absorption bandwidth (EAB) of 4.17 GHz [20]. In addition, polymer-based functionalization is also a magnificent method to improve the dielectric "genes" of CNT [21-23]. For instance, Liu et al. utilize cellulose nanofibrils as efficient surfactants and dielectric modulators, leading to stable dispersion and good impedance matching [24]. Despite such progress, achieving ultralow density remains challenging for CNT-based EMWA materials.

Fortunately, multicomponent aerogels with three-dimensional (3D) porous structures exhibit brilliant EMWA performance [3, 25]. Firstly, the 3D porous structures contain plenty of air in aerogels, resulting in the impedance approaching air, which allows more incident EMW to follow the pores into the aerogel interior [26]. Additionally, the tortuous pores and

walls extend the transmission path of EMW and provide abundant interfaces for EMW attenuation via multiple scattering [27]. For example, an ultralight N-doped graphene aerogel with atomically dispersed cobalt exhibited an RL_{min} of -49.13 dB and an EAB of 4.24 GHz [28]. Above all, the anisotropic porous structures are further designed with diverse EMW loss capabilities in different directions, thereby regulating better EMWA performances [29]. For instance, Ni et al. prepared anisotropic polyimide/carbon nanotube composite aerogels with oriented channel structures [11]. The composite aerogels showed an RL_{min} of −52 dB in the vertical direction of oriented channels, but only −11 dB in the paralleled direction of channels. However, it is difficult for previously reported aerogels to simultaneously satisfy the requirements of lightweight, high thermal stability, low thermal conductivity, high RL_{min}, and wide EAB. Because there is a conflict between low thermal conductivity and excellent EMWA performance in achieving lightweight aerogels. Aerogels with low thermal conductivity usually require less filler to increase porosity. Nevertheless, due to the agglomeration of EMW absorbers, aerogels with excellent EMWA performance often require more EMW absorbers [30]. Therefore, a method is needed to avoid the agglomeration of EMW absorbers and construct networks with fewer EMW absorbers.

Aramid nanofiber (ANF), prepared from poly-p-phenylene terephthamide (PPTA), demonstrates exceptional dispersion stability, mechanical strength, high-temperature stability, and flame resistance [31]. Furthermore, the electrostatic repulsion and hydrogen bonds of ANF between molecular chains strengthen the interfacial interaction with other matrices. In addition, ANF with a large aspect ratio and branched structure can load carbon nanofiller to build 3D

networks at a lower filling amount [32]. For instance, Wang et al. took advantage of 0.4 wt% ANF to support 1.6 wt% graphene nanosheets and obtained a conductive fiber via wet-spinning [33]. At present, the application of ANF in EMWA materials still needs to be developed.

In this work, a honeycomb-like carboxylic multi-walled carbon nanotube/aramid nanofiber (c-MWCNT/ANF) aerogel was fabricated through sol-gel transition, unidirectional freezing, and freeze-drying. ANF with strong alkaline-induced electrostatic repulsion improves the dispersity of c-MWCNT. Subsequently, H_2O as a proton donor protonates c-MWCNT and ANF to form interfacial hydrogen-bond networks. The interconnected hydrogen-bond networks between c-MWCNT and ANF fix the 3D skeleton of c-MWCNT/ANF and realize the sol-gel transition of c-MWCNT/ANF suspension. What's more, ANF as a non-conductor is introduced to edit the conduction "genes" of c-MWCNT. Meanwhile, the interfacial hydrogen bonds between c-MWCNT and ANF enhance the polarization "genes" [34]. As a result, the anisotropic c-MWCNT/ANF aerogel with a low density of 26.2 g cm^{-3} displays an RL_{min} of −60.43 dB and an EAB of 5.34 GHz along the vertical direction. In addition, the c-MWCNT/ANF aerogel possesses excellent thermal insulation and flame resistance, these superior advantages will improve the reliability of c-MWCNT/ANF aerogels under complicated environments.

2. Material and methods

2.1. Materials

PPTA thread (Kevlar 49) was purchased from DuPont, USA. MWCNT (10 ~ 30 nm in diameter, 10 ~ 30 μm in length, 98% purity) were obtained from Chengdu Organic Chemical

Co. Ltd, Chinese Academy of Sciences. Dimethyl sulfoxide (DMSO) was supplied by Aopu Sheng Chemical Co. Ltd, Tianjin. Potassium hydroxide (KOH) was provided by Mainland Chemical Reagent Factory, Tianjin. Deionized (DI) water was produced by a water purification system (UPH-IV-5TNP, ULUPURE, China).

2.2. Preparation of carboxylic multi-walled carbon nanotube (c-MWCNT) and ANF solutions

c-MWCNT solution was prepared by the following method [17]. Firstly, 2g pristine MWCNT was added into 400 mL H_2SO_4/HNO_3 mixed acid solution (3:1 by volume) and reacted while stirring at 60 °C for 120 min. Then, the suspension was filtered and washed with deionized water until it reached a neutral pH. Whereafter, the powders were dried at 60 °C under vacuum for 12 h. Finally, 1.796 g of c-MWCNT and 80 mL of DMSO were mixed by an ultrasonic cell disruptor for 15 min to obtain a 2 wt% c-MWCNT/DMSO solution.

ANF solution was prepared by the previous method [35], 6.876 g of KOH and 6.876 g of PPTA thread were added into 300 mL of DMSO, which was magnetically stirred for 5 days at room temperature to obtain a 2 wt% ANF/DMSO/KOH solution.

2.3 Preparation of c-MWCNT/ANF aerogels

According to Table 1, 20, 30, 40, and 45 g of 2wt% c-MWCNT/DMSO solution were added into 40, 30, 20, and 15 g of 2wt% ANF/DMSO/KOH solution, respectively. Then, these mixtures were further stirred for 6 h to obtain a homogenous c-MWCNT/ANF/DMSO/KOH solution. 30 g of c-MWCNT/ANF/DMSO/KOH solution was poured into customized Teflon

molds with copper base. Subsequently, place the molds in DI water for 3 days to exchange the solvent system, and replace the water every 12 h. DI water, as a proton donor, protonated c-MWCNT and ANF during solvent replacement. After substituting the DMSO/KOH with the H_2O, c-MWCNT/ANF formed hydrogels due to the construction of hydrogen-bond networks between c-MWCNT and ANF. For the design of anisotropic microstructure, the method of unidirectional freeze cast was selected to erect oriented holes by controlling the growth direction of ice crystals. The procedure was as follows: the bottom of c-MWCNT/ANF hydrogels touched a 5 cm height copper column, and the copper column was half submerged in liquid nitrogen for 20 min. Subsequently, the completely frozen samples were dried in a freeze dryer for 72 h, resulting in the final c-MWCNT/ANF aerogels.

Table 1. The ratio of c-MWCNT/DMSO solution and ANF/DMSO/KOH solution.

Sample	2 wt% c-MWCNT/DMSO solution (g)	2 wt% ANF/DMSO/KOH solution (g)	Label
1	20	40	C1A2
2	30	30	C1A1
3	40	20	C2A1
4	45	15	C3A1

2.4 Characterization

The morphology and EDS mapping of c-MWCNT/ANF aerogels were investigated by scanning electron microscope (SEM, SU-5000, Hitachi, Japan) at an accelerated voltage of 20

kV. The diameter of c-MWCNT was observed using a transmission electron microscope (TEM, JEM-F200, JEOL, Japan). The diameter of ANF was measured with atomic force microscopy (AFM, Smart SPM, AIST-NT, USA). Fourier transform infrared spectroscopy (FTIR, Spectrum Two, PerkinElmer, UK) was applied to characterize the functional groups and hydrogen bonds of c-MWCNT and ANF. An X-ray diffractometer (XRD, Empyrean, PANalytical, Netherlands) was used to determine the crystal lattices with a scanning rate of 5°/min and a range from 10° to 80° (2θ). The chemical structures of c-MWCNT and ANF were investigated using a Raman imaging microscope spectrometer (inVia-Reflex, RENISHAW, UK) with a laser source wavelength of 532 nm. The element compositions of specimens were identified via X-ray photoelectron spectroscopy (XPS, ESCALAB 250Xi, Thermo-Fisher, USA) using a monochromatic Al K_α source.

Electrical conductivities were measured through a 4-point probe resistivity measurement system (RT-70V, Napson, Japan). Thermal conductivities were characterized using a hot disk (Hot Disk, TPS 2500S, Sweden). Compression tests were performed by a universal testing machine (Instron, USA) with a strain of 30% and a compression speed of 1 mm min^{-1}. The thermal stability of samples was tested by employing a thermogravimetric analyzer (TGA 1, Mettler Toledo, Switzerland) under a N_2 atmosphere, with a heating rate of 10 ℃/min from 40 ℃ to 1000 ℃. The relative complex permittivity (ε_r) and permeability (μ_r) in the frequency range of 2–18 GHz were measured using a vector network analyzer (E5071C, Agilent, USA) via the coaxial line method. The aerogels were infused with paraffin (the ratio of aerogel to paraffin was controlled at 5 wt% to 95 wt%) and cut into a cylinder with an outer diameter of

7.0 mm and an inner diameter of 3.04 mm. The reflection loss (RL) values were calculated according to the transmission line theory.

3. Results and discussion

3.1 Fabrication strategy and mechanism

Although MWCNT has fantastic prospects as EMWA materials, their poor dispersibility, difficulty in mold-shaping, and impedance mismatch limit their application. In this work, ANF is introduced to address these issues successfully. Comparing the stability of c-MWCNT and c-MWCNT/ANF suspensions in the DMSO/KOH solvent system, it is evident that pure c-MWCNT suspension tends to aggregate and settle at the bottom of the bottle in a short time (Fig. S1a). Nevertheless, the c-MWCNT/ANF suspension maintains a stable state even after being left for 2 h. This stability is attributed to the deprotonation of ANF in the alkaline solvent system, resulting in strong electrostatic repulsion between molecular chains that prevents c-MWCNT from aggregating. In the alkaline solution of DMSO/KOH, c-MWCNT forms numerous ionized carboxyl groups ($-COO^-$), and ANF forms numerous deprotonated amino groups ($-N^--$). Both c-MWCNT and ANF carry negative charges, thus there is a strong electrostatic repulsion between c-MWCNT and ANF. However, after DMSO/KOH is replaced with H_2O through the solvent exchange, $-COO^-$ and $-N^--$ acquiring protons from H_2O convert into -COOH and -NH-. Finally, interfacial hydrogen-bond networks are formed between -COOH of c-MWCNT and -CONH- of ANF. Fig. 1a illustrates the formation mechanism of hydrogen bonds between c-MWCNT and ANF. As shown in Fig. S1b, the c-MWCNT/ANF suspension transforms into a gel block, constructing a homogeneous 3D skeleton of c-

MWCNT/ANF.

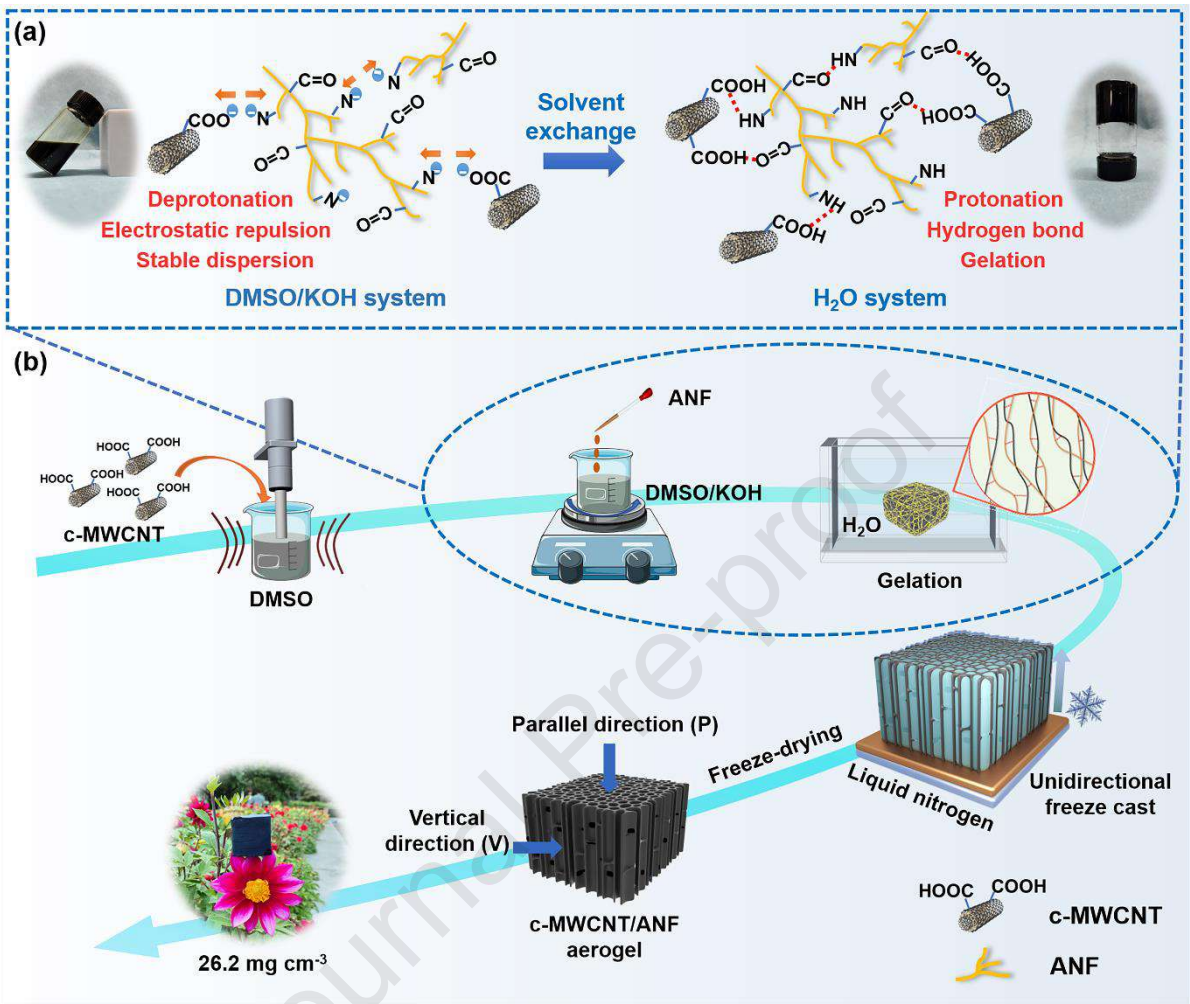

Fig. 1. Schematic illustration: (a) the mechanism of interfacial interaction between c-MWCNT and ANF; (b) the fabrication strategy of c-MWCNT/ANF aerogel.

Fig. 1b illustrates the preparation process of c-MWCNT/ANF aerogels, where a unidirectional freeze cast and freeze-drying method are applied to fabricate oriented channels inside aerogels. The composite aerogels, with ultralow density (26.2 mg cm^{-3}), can stand on a flower (Fig. 1b and S2).

3.2 Composition analysis

The chemical functional group and hydrogen-bond interaction were characterized by FTIR spectra. By comparing the original MWCNT and c-MWCNT spectra, c-MWCNT with carboxyl groups are confirmed via the stretching vibration of O-H and C=O at 3438 cm^{-1} and 1626 cm^{-1}, respectively (Fig. S3). These functional groups are beneficial for polarization under high-frequency EMW. For ANF aerogel, the stretching vibration of N-H and C=O is at 3331 cm^{-1} and 1652 cm^{-1}, respectively [36]. However, the stretching vibration of N-H (3317 cm^{-1}) and C=O (1643 cm^{-1}) in c-MWCNT/ANF aerogel exhibits a lower wavenumber than in the ANF aerogel, indicating hydrogen-bond interaction between c-MWCNT and ANF (Fig. 2a).

The XRD patterns in Fig. 2b validate the composition and crystal structure of c-MWCNT powder, ANF aerogel, and c-MWCNT/ANF aerogel. The diffraction peaks of c-MWCNT/ANF aerogel are located at 20.79°, 23.39°, 26.18°, and 43.12°, corresponding to the (110), (200), (002), and (100) crystal lattices, respectively. These diffraction peaks are consistent with the c-MWCNT powder and ANF aerogel.

The Raman spectra of c-MWCNT powder, ANF aerogel, and c-MWCNT/ANF aerogel were exhibited in Fig. 2c. D peak and G peak represent the vibration of amorphous and crystalline carbon atoms, respectively [6]. The intensity ratio of the D and G peaks (I_D/I_G) can be used to evaluate the disorder degree of structural defect of carbon materials. The I_D/I_G of c-MWCNT powder is 1.11, verifying abundant structural defects in c-MWCNT. However, the I_D/I_G of c-MWCNT/ANF aerogel decreases to 1.04, probably because the oriented channels of aerogel promote the orderly distribution of c-MWCNT.

The element content and composition of material surfaces were explored by XPS [37]. As

shown in Fig. 2d and Table S1, c-MWCNT powders have 91.7% C, 6.35% O, and 1.96% N. The surface of c-MWCNT/ANF aerogel includes 73.66% C, 16.24% O, and 10.1% N, in which the element content of O and N increases significantly due to the addition of ANF. To further confirm the functional groups and interfacial hydrogen bond of the c-MWCNT/ANF aerogel, we investigated the XPS C1s, O1s, and N1s spectra. Fig. 2e illustrates the XPS C1s spectra, and the peaks at 285.7, 286.4, 288.2, and 290.9 eV correspond to -C-N-, -C-O-, -C=O-, and π-π interactions, respectively [38]. Fig. 2f exhibits the XPS O1s spectra, and the peaks at 531.5 and 532.6 eV can be ascribed to -C=O- and -C-O-, respectively [39]. By comparing the XPS N1s spectrum of ANF and c-MWCNT/ANF aerogel, the interfacial hydrogen bond between c-MWCNT and ANF is further verified. As shown in Fig. S4, the N1s spectra of ANF aerogel has a single peak at 399.5 eV, indicating that nitrogen atoms in ANF aerogel are in the same chemical state. However, the N1s spectra of c-MWCNT/ANF aerogel can be deconvoluted into two peaks at 399.5 and 400.0 eV, respectively (Fig. 2g). The new chemical state (400.0 eV) of nitrogen atoms in c-MWCNT/ANF illustrates that -CONH- of ANF forms hydrogen bonds with -COOH of c-MWCNT [40]. The hydrogen bonds between ANF and c-MWCNT can enhance the polarization loss ability of aerogel under high-frequency EMW.

Overall, the FTIR, XRD, Raman, and XPS results verified the successful integration of c-MWCNT and ANF.

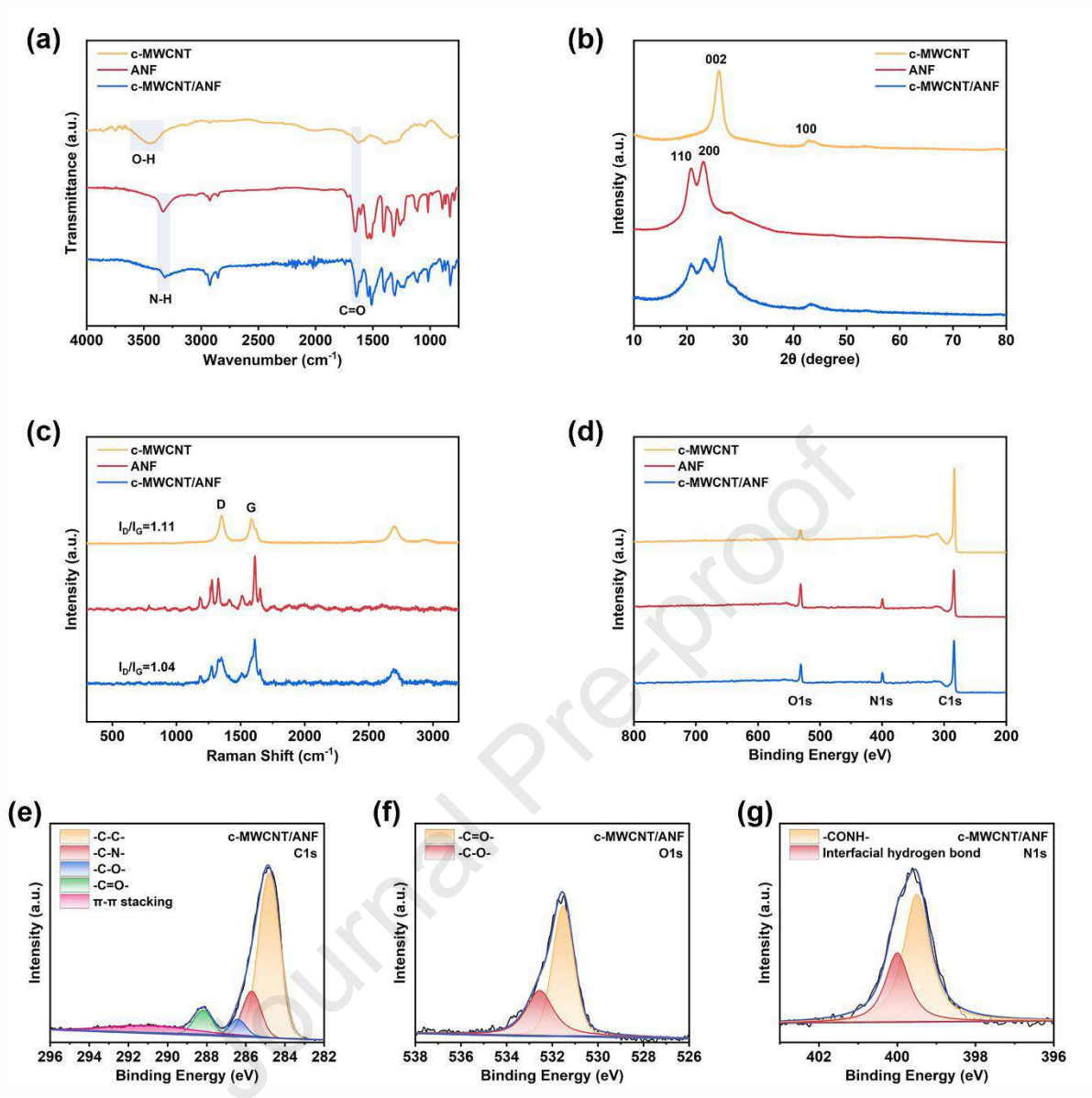

Fig. 2. Composition analysis: (a) FTIR spectra; (b) XRD spectra; (c) Raman spectra, (d) XPS spectra; (e) XPS C1s spectra of c-MWCNT/ANF aerogel; (f) XPS O1s spectra of c-MWCNT/ANF aerogel; (g) XPS N1s spectra of c-MWCNT/ANF aerogel.

3.3 Structural and morphological analysis

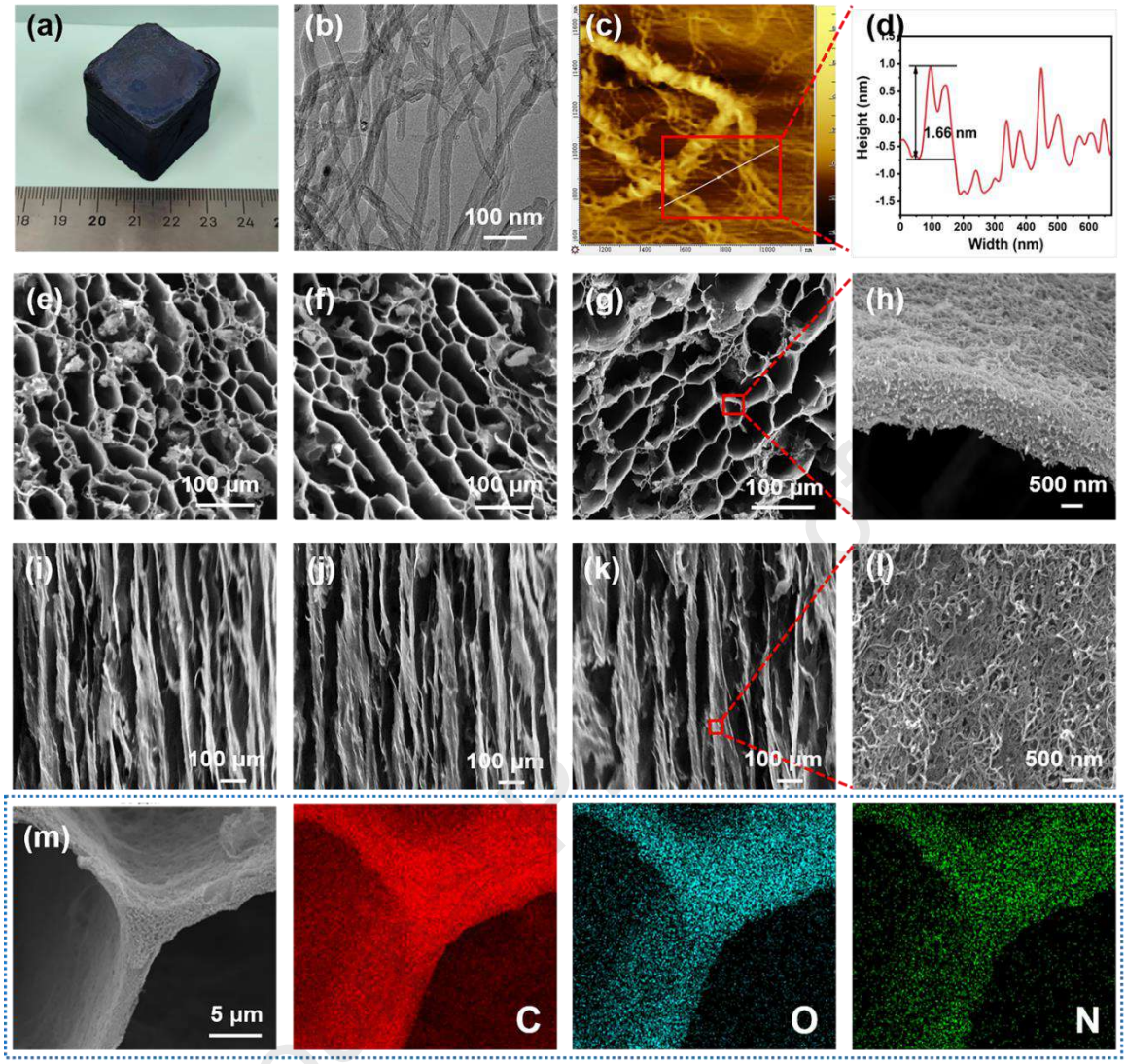

Fig. 3. Structural and morphological analysis: (a) Digital photo of a c-MWCNT/ANF aerogel; (b) c-MWCNT corresponding TEM image; (c, d) ANF corresponding AFM image and height; (e-h) SEM photographs of C1A1, C2A1, C3A1 aerogels in the parallel direction; (i-l) SEM photographs of C1A1, C2A1, C3A1 aerogels in the vertical direction; (m) element mapping images of the c-MWCNT/ANF aerogel.

Fig. 3a shows a c-MWCNT/ANF aerogel photo with a size of about 2.5 × 2.5 × 2.8 cm. TEM and AFM were applied to observe the morphology and diameter of c-MWCNT and ANF.

c-MWCNT has a large aspect ratio, and the average diameter is approximately 24 nm (Fig. 3b). ANF exhibits a branched structure, and the corresponding diameter is about 1.66 nm (Fig. 3c and d).

The microstructure of hybrid aerogels was confirmed by SEM. Owing to the unidirectional freezing method, the c-MWCNT/ANF aerogels show an anisotropic-oriented porous structure. For convenience, the anisotropic c-MWCNT/ANF aerogels were denoted as (P/V)-CxAy, where P and V represented the parallel direction and vertical direction of ice crystal growth, C and A represented c-MWCNT and ANF, x and y represented the relative mass ratio of c-MWCNT to ANF in composite aerogels, respectively. For comparison, the C2A1 aerogel with random holes was prepared by placing the c-MWCNT/ANF hydrogel into the fridge and then freeze-drying. The sample was denoted as R-C2A1. From the perspective of the parallel direction of ice crystal growth (Fig. 3e-g), the P-C1A1, P-C2A1, and P-C3A1 aerogels are composed of a honeycomb-like structure. The wall thickness of the oriented channel is approximately 0.91 μm (Fig. 3h), and the average pore sizes are from 40.4 to 51.2 μm (Fig. S5). From the perspective of the vertical direction of ice crystal growth (Fig. 3i-l), the V-C1A1, V-C2A1, and V-C3A1 aerogels are composed of aligned layered structure, which is beneficial for the polarization ability of the aerogel [41]. The R-C2A1 aerogel shows a random channel structure (Fig. S6). Besides, the element mapping images of composite aerogel were collected to estimate the distribution situation of c-MWCNT and ANF. As displayed in Fig. 3m, the homogeneous distribution of C, O, and N elements in the aerogel wall further verifies the successful combination of c-MWCNT and ANF.

3.4 Anisotropic EMWA performance

The permittivities (ε' and ε'') and the permeabilities (μ' and μ'') were measured to investigate the EMWA performance of aerogels. Since aerogels do not contain magnetic components, the μ' is approximately one, and the μ'' is close to zero. Thus, the permeabilities are not discussed in this section.

As displayed in Fig. 4a and b, both ε' and ε'' in parallel and vertical directions present a growing tendency with a ratio of c-MWCNT increase, demonstrating an enhanced electronic conduction path. Furthermore, the vertical direction of aerogels reveals larger ε' and ε'' values than the parallel direction (Fig. 4a, b and S10a, b). This discrepancy in electromagnetic parameters is probably due to unimpeded channels along the parallel direction allowing for the escape of the incident EMW [11, 42]. By contrast, vertically incident EMW needs to traverse numerous channel walls, and c-MWCNT/ANF aligned in the walls produces strong electronic polarization (Fig. S7). Meanwhile, multiple scattering and reflection in the vertical direction boost the loss capacity. As demonstrated in Fig. 4c, there are relaxation peaks for $\tan\delta_\varepsilon$ ($\tan\delta_\varepsilon = \varepsilon''/\varepsilon'$) curves in the high-frequency regions, indicating the c-MWCNT/ANF composite aerogels exhibit excellent dielectric loss. Moreover, the anisotropic aerogel displays larger $\tan\delta_\varepsilon$ values than the random aerogel at the same filler ratio (Fig. S8c), which proves that the anisotropic structure has a better dielectric loss capability.

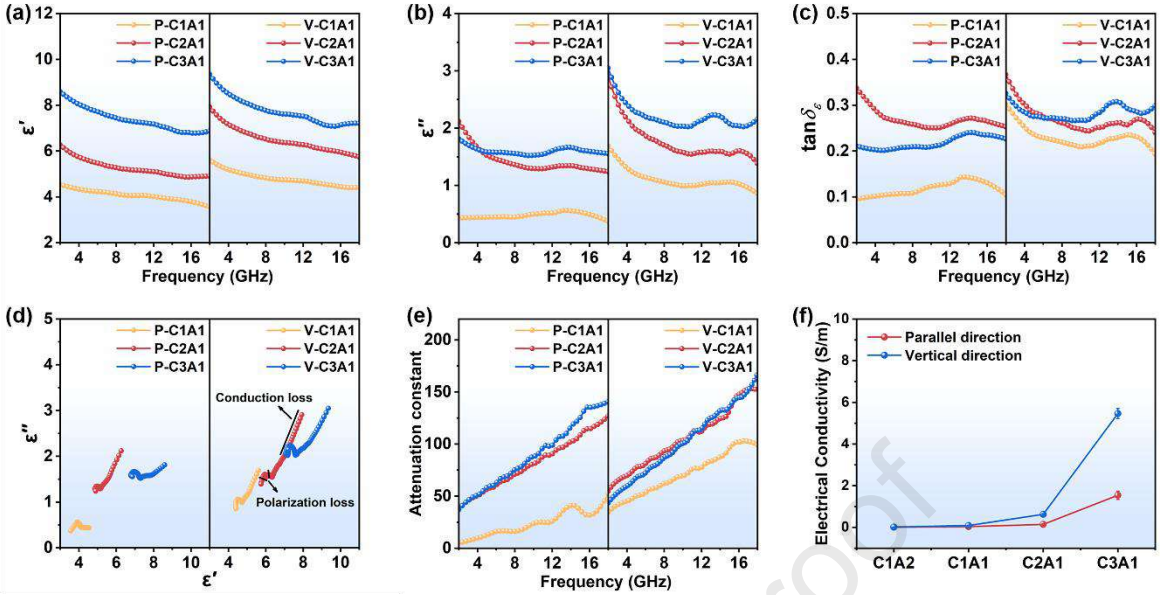

Fig. 4. Electromagnetic parameters versus frequency of c-MWCNT/ANF aerogels in the parallel and vertical direction: (a) real part of permittivity, (b) imaginary part of permittivity, (c) dielectric loss tangent; (d) Cole-Cole curves of c-MWCNT/ANF aerogels; (e) attenuation constant of c-MWCNT/ANF aerogels; (f) electrical conductivities of composite aerogels.

Cole-Cole curves were plotted to analyze the phenomenon of polarization relaxation and conduction loss, according to equations 1, 2, and 3:

$$\varepsilon' = \varepsilon_\infty + \frac{\varepsilon_s - \varepsilon_\infty}{1 + \omega^2\tau^2} \tag{1}$$

$$\varepsilon'' = \frac{\varepsilon_s - \varepsilon_\infty}{1 + \omega^2\tau^2}\omega\tau + \frac{\sigma}{\omega\varepsilon_0} \tag{2}$$

$$\left(\varepsilon' - \frac{\varepsilon_s + \varepsilon_\infty}{2}\right)^2 + (\varepsilon'')^2 = \left(\frac{\varepsilon_s - \varepsilon_\infty}{2}\right)^2 \tag{3}$$

Here, ε_∞ represents the relative permittivity at a high-frequency limit, ε_s represents the static permittivity, ω represents the angular frequency, τ represents the polarization relaxation time, and σ represents the conductivity [43]. When EMW passes through the c-MWCNT/ANF aerogels, the semicircular parts of the curves confirm the presence of multiple

polarization relaxation, and the linear segments represent the conduction loss (Fig. 4d and S9a). Furthermore, the conduction loss shows noticeable variations compared with the polarization loss as increasing the ratio of c-MWCNT (Fig. 4d), and the length of the linear segment reaches the maximum in C2A1 aerogel Additionally, V-C2A1 aerogel demonstrates superior conduction loss compared to P-C2A1 and R-C2A1 aerogel at the same ratio of c-MWCNT to ANF (Fig. S9a). Above all, the V-C2A1 aerogel yields the most comprehensive conduction and polarization loss effect.

The attenuation constant (α) is a vital factor in evaluating the capability of the sample to convert EMW energy into other forms of energy (equation. 4).

$$\alpha = \frac{\sqrt{2}}{c}\pi f \times \sqrt{(\mu''\varepsilon'' - \mu'\varepsilon') + \sqrt{(\mu''\varepsilon'' - \mu'\varepsilon')^2 + (\mu'\varepsilon'' + \mu''\varepsilon')^2}} \quad (4)$$

Where f is the EMW frequency, and c is the speed of light in a vacuum [44]. The α values of c-MWCNT/ANF aerogels gradually increase with the rising c-MWCNT content and frequency (Fig. 4e). At the same filler ratio, the V-C2A1 aerogel demonstrates larger α values than the P-C2A1 and R-C2A1 aerogel, indicating that the V-C2A1 aerogel has a better EMW loss capacity (Fig. S9b).

Fig. 4f shows the electrical conductivities of c-MWCNT/ANF composite aerogels. As the contents of c-MWCNT increase, the conductivities of the aerogels rise in both parallel and vertical directions, indicating that conductive networks gradually form in the composite aerogel. Additionally, the conductivities in the vertical direction are slightly larger than in the parallel direction, demonstrating anisotropic conductive performances. The conductive networks of c-MWCNT can produce conduction loss, building a solid foundation for the composite aerogels

to attenuate the incident EMW.

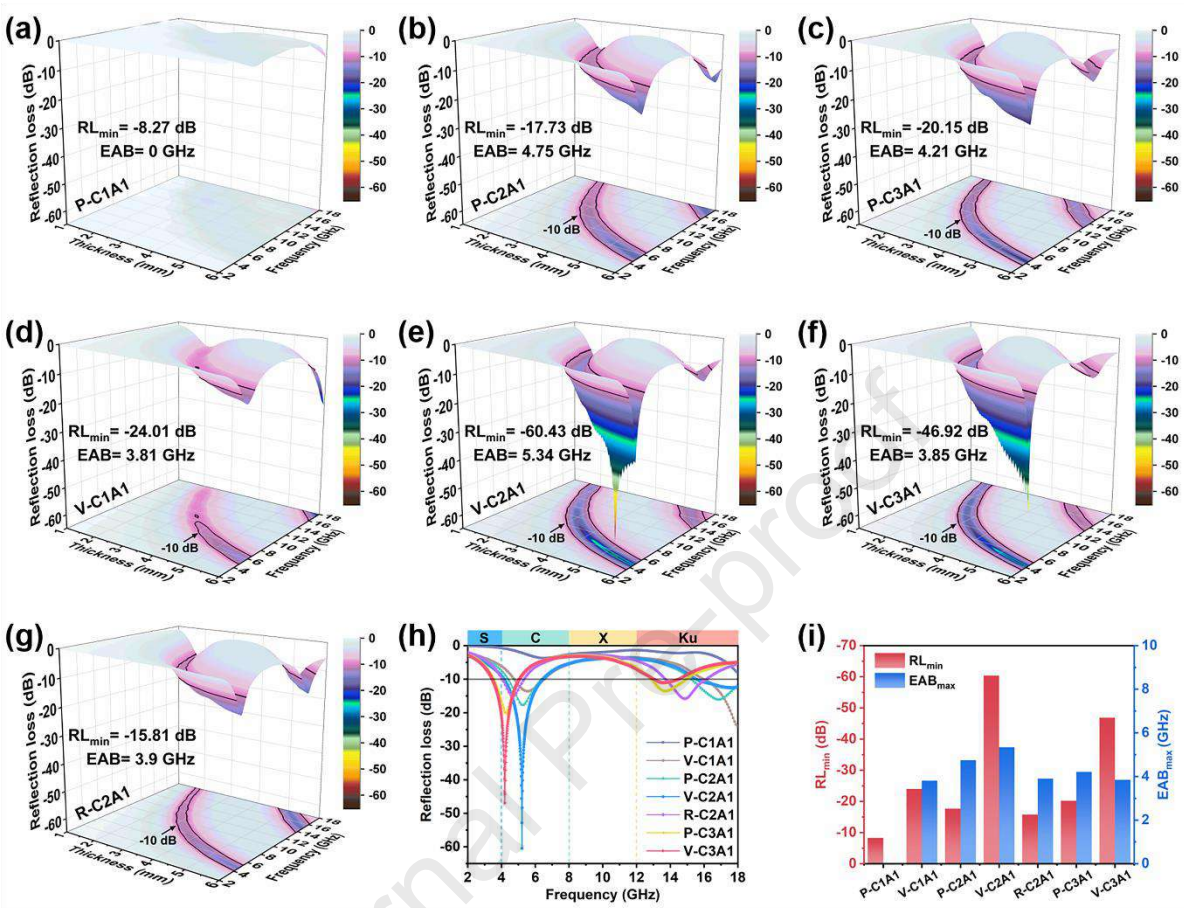

Fig. 5. 3D RL plots: (a) C1A1, (b) C2A1, (c) C3A1 composite aerogels in the parallel direction; (d) C1A1, (e) C2A1, (f) C3A1 composite aerogels in the vertical direction; (g) C2A1 composite aerogels with a random structure. (h) 2D RL_{min}-f curves, (i) RL_{min} and EAB of composite aerogels with different c-MWCNT to ANF ratios and structures.

The RL and EAB values were applied as assessment metrics for the EMWA performance of as-prepared aerogels. Based on transmission line theory, the RL values were calculated according to the following equations 5 and 6:

$$Z_{in} = Z_0\sqrt{\frac{\mu_r}{\varepsilon_r}}\tanh\left[j\left(\frac{2\pi f d}{c}\sqrt{\mu_r\varepsilon_r}\right)\right] \quad (5)$$

$$RL(dB) = 20\lg|(Z_{in} - Z_0)/(Z_{in} + Z_0)| \quad (6)$$

Where Z_{in} is the input impedance of the absorber surface, Z_0 is the impedance of free space, and d is the thickness. ε_r ($\varepsilon_r = \varepsilon' - j\varepsilon''$) and μ_r ($\mu_r = \mu' - j\mu''$) are complex permittivity and complex permeability, respectively [45]. Generally, EAB indicates the frequency band corresponding to the RL values less than -10 dB.

The RL curves of 3D and 2D mapping are shown in Fig. 5 and S10. P-C1A2 and V-C1A2, due to low c-MWCNT content, are not able to absorb EMW effectively (Fig. S10c and d). By comparing P-C1A1 and V-C1A1 aerogel, P-C1A1 aerogel with an RL_{min} value of only -8.27 dB and an EAB of 0 GHz exhibits negligible EMWA performance (Fig. 5a). However, V-C1A1 aerogel, at the same ratio of c-MWCNT to ANF, displays an RL_{min} value of -24.01 dB and an EAB of 3.81 GHz (Fig. 5d). The variation of EMWA performance between the P-C1A1 and V-C1A1 aerogel confirms the influence of anisotropic structure. Besides, when comparing the P-C2A1, V-C2A1, and R-C2A1 aerogels (Fig. 5b, e, and g), it is evident that the aerogel along the vertical direction has a better EMWA performance than the parallel direction and random structure. Furthermore, impedance matching and dielectric loss achieve a balance in the V-C2A1 aerogel with the proportion adjustment of c-MWCNT and ANF [26]. Thus, compared to other aerogels, the V-C2A1 aerogel with a thickness of 5.3 mm can reach the optimal RL_{min} of -60.43 dB at 5.22 GHz and wide EAB of 5.34 GHz (Fig. 5e, h and i).

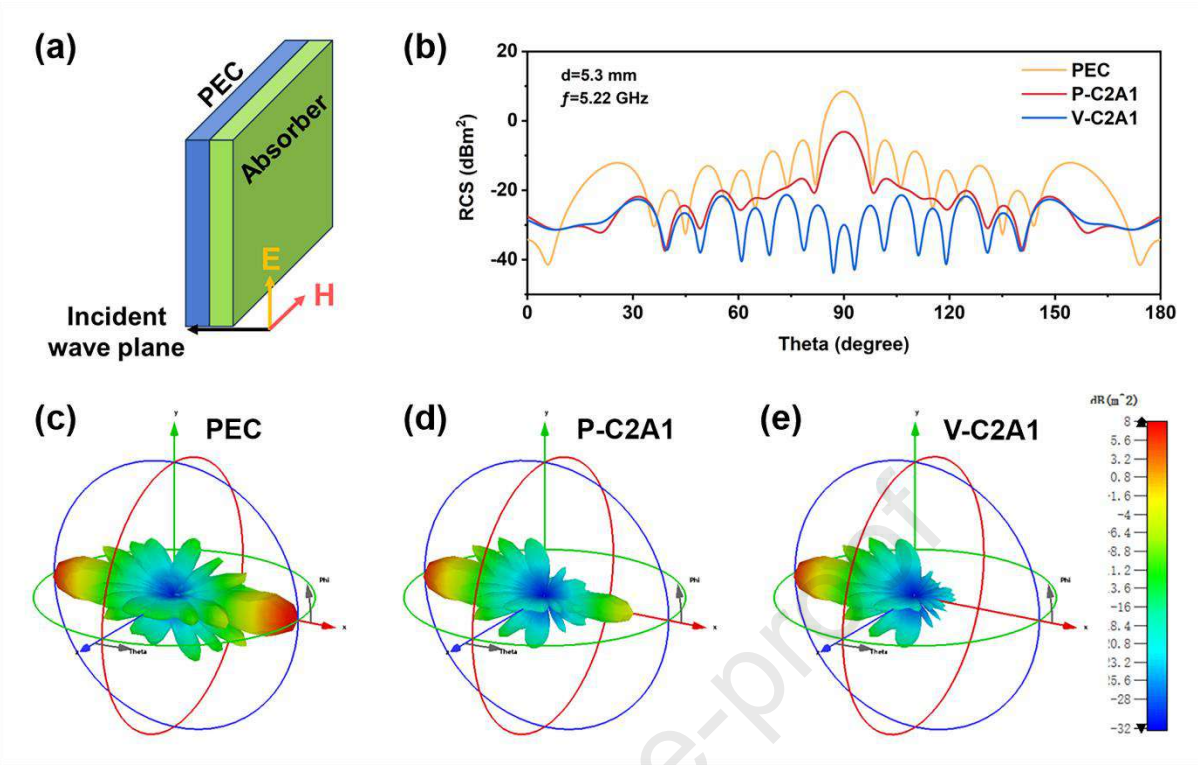

Fig. 6. (a) The simulation model: a PEC plate coated with c-MWCNT/ANF absorber (b) 2D RCS simulation curves of samples at different observation angles; 3D RCS scattering signals of (c) PEC plate, (d) PEC plate coated with P-C2A1, (e) PEC plate coated with V-C2A1.

To simulate the EMWA performance of c-MWCNT/ANF absorber in practical application scenarios, perfect electric conductor (PEC) plates (size: 200 × 200 mm^2) coated with c-MWCNT/ANF absorber were constructed in CST Studio Suite 2022 (Fig. 6a). The thickness of absorber was set as 5.3 mm, the test frequency was 5.22 GHz, and EMW entered from the vertical direction of PEC/absorber plates. The 2D radar cross section (RCS) simulation curves of samples for observation angles from 0° to 180° are exhibited in Fig. 6b. At an observation angle of 90°, the RCS value of V-C2A1 (-29.59 dBm^2) is lower than pure PEC (8.55 dBm^2) and P-C2A1 (-3.07 dBm^2). In addition, the 3D RCS scattering signal of V-C2A1 also shows a

lower intensity than pure PEC and P-C2A1 (Fig. 6c-e), indicating that V-C2A1 coating has the best EMWA performance. The RCS simulation results are consistent with the RL plots.

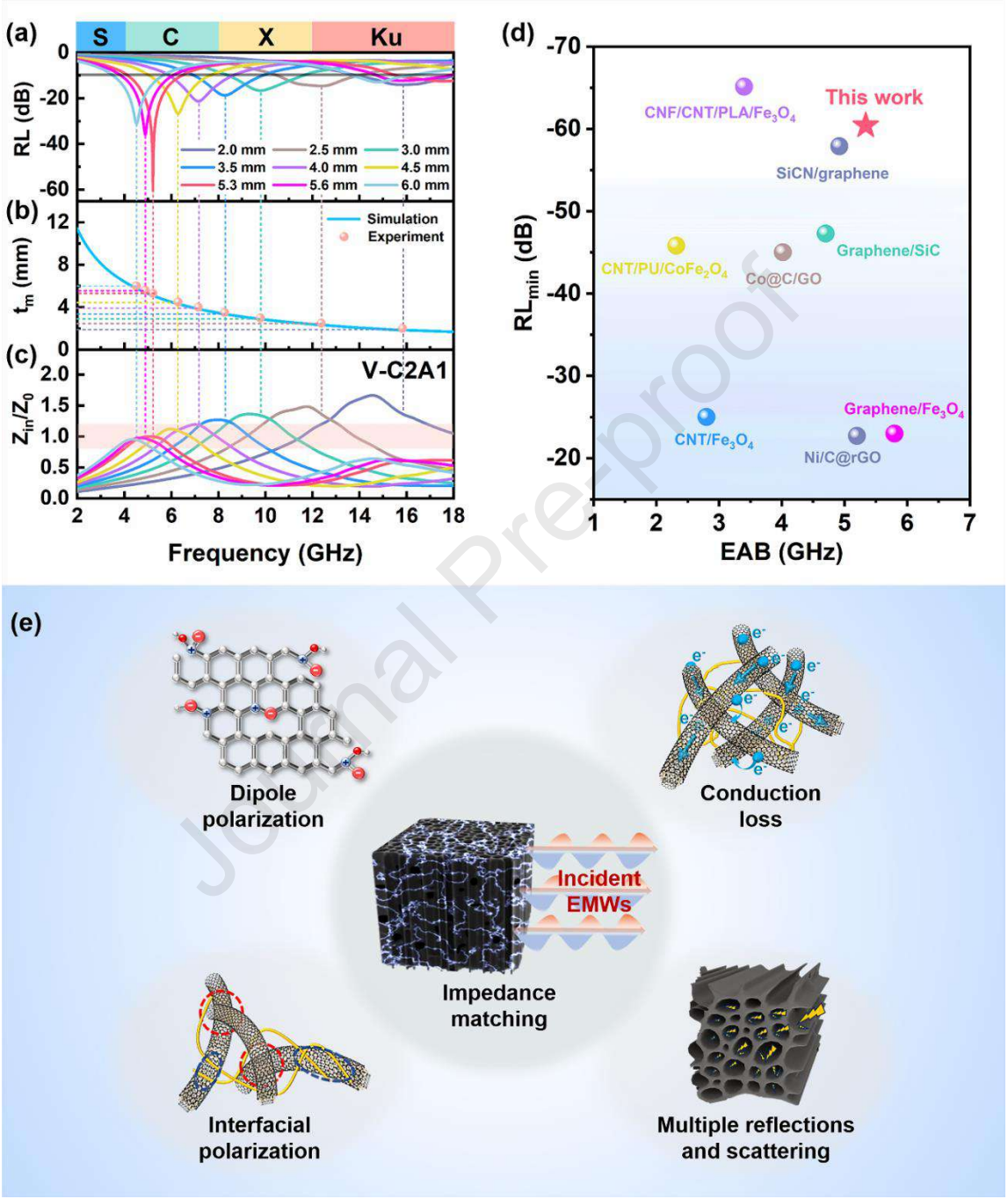

Fig. 7. (a-c) RL/t_m/Z-f curves of the V-C2A1 aerogel; (d) comparison of RL_{min} and EAB with previously reported carbon-based aerogel EMWA materials; (e) schematic illustrations of EMWA mechanism of c-MWCNT/ANF aerogel.

By adjusting the thickness of V-C2A1 aerogel, the EAB can cover the entire C, X, and Ku frequency bands (Fig. 7a). Furthermore, as the thickness increases, the adsorption peaks of RL_{min} shift toward the lower frequency region, which can be justified by the simulation of quarter-wavelength attenuation (equation 7).

$$t_m = \frac{n\lambda}{4} = \frac{nc}{4f_m\sqrt{|\mu_r||\varepsilon_r|}}; \text{ (n = 1, 3, 5, …)} \quad (7)$$

where λ is the EMW wavelength, f_m is the frequency at RL peak, and t_m is the sample thickness [46]. When the incident EMW is transmitted to the surface of aerogel, if the thickness of the aerogel is equal to n/4 of the EMW wavelength (where n is an odd number), the incident EMW at the air-aerogel interface and the reflected EMW at the aerogel-metal substrate will cancel each other, enhancing the EMWA performance of the aerogel. Fig. 7a and b demonstrate that the experimental results are consistent with the curve of theoretical simulation of quarter-wavelength attenuation. In addition, impedance matching is a vital factor in determining the EMWA performance, and the normalized characteristic impedance (Z_{in}/Z_0) is applied to assess the impedance matching degree of aerogel. When the Z_{in}/Z_0 is close to 1, EMW can enter the aerogel without reflection, revealing an ideal impedance-matching state [47]. Fig. 7c shows that the Z_{in}/Z_0 value of V-C2A1 aerogel is between 0.8 and 1.2 in a broad frequency region. Thus, the V-C2A1 aerogel has a large EAB.

Achieving strong EMWA with smaller RL_{min} and more extensive EAB is the fundamental target for advanced EMWA materials. Compared with previously reported carbon-based aerogel EMWA materials, the c-MWCNT/ANF aerogels exhibit an impressive EMWA performance (Fig. 7d and Table S2).

Fig. 7e illustrates possible EMWA mechanisms for c-MWCNT/ANF aerogel. Firstly, the carboxyl and intrinsic defects of c-MWCNT can cause dipole pairs under high-frequency EMW. Because the rotation of the dipole pairs lags behind the high-frequency EMW, it consumes EMW energy [48]. Secondly, electron migration occurs within c-MWCNT. and electron hopping is induced by the lap joint between c-MWCNTs, which promotes the conduction loss of aerogel [49]. Thirdly, the c-MWCNT/ANF with entanglement heterojunctions could provide plenty of interfacial hydrogen bonds, which generates interface polarization effects. Fourthly, anisotropic aerogel along the vertical direction creates abundant walls, significantly prolonging the EMW transmission path and leading to multiple reflections and scattering. Additionally, ANF dramatically optimizes the impedance mismatch and electromagnetic parameters of aerogel by regulating the dielectric "genes" of c-MWCNT.

3.5 Thermal insulation and flame resistance

Besides outstanding EMWA performance, the versatility of c-MWCNT/ANF aerogel was further investigated, including thermal insulation and flame resistance. As displayed in Fig. 8a and b, commercial PU foam, P-C2A1, and V-C2A1 aerogels with the same thickness were placed on a 100 ℃ heating platform for 600 s, and their corresponding surface temperature is 41.1 ℃, 45.8 ℃, and 38.2 ℃, respectively. The excellent thermal insulation performance is attributed to the strong skeleton of c-MWCNT/ANF, which can establish 3D porous aerogel with 98.4% porosity (Fig. S11). Moreover, the V-C2A1 aerogel shows a lower surface temperature than the P-C2A1 aerogel, indicating that oriented pores affect the thermal insulation behaviors of aerogel. As shown in Fig. 8c, the P-C2A1 aerogel with thermal

conductivity of 45.7 mW m^{-1} K^{-1} and the V-C2A1 aerogel with thermal conductivity of 30.7 mW m^{-1} K^{-1} also prove that C2A1 aerogel has a better thermal insulating property along the vertical direction. Fig. 8d exhibits the mechanism of heat transfer along the parallel and vertical directions of anisotropic aerogel [29, 50]. The red arrows represent the gas heat transfer in aerogel. Due to its anisotropic structure, the aerogel has more pore walls along the vertical direction than along the parallel direction. The heat flow will be obstructed by more walls when transmitting along the vertical direction. However, the heat flow can quickly propagate through the tubular structure along the parallel direction. Thus, the gas heat transfer along the parallel direction of aerogel is more efficient than the vertical direction of aerogel. Besides, solid heat transfer is also a form of heat conduction, the yellow arrows represent the path of heat flow through the skeleton of aerogel. The parallel direction has a shorter solid heat transfer path than the vertical direction. Meanwhile, the pore walls can also dissipate heat energy through radiant heat transfer (green arrows). To summarize, the heat transfer rate along the parallel direction is faster, thus the aerogel has a greater thermal insulating property along the vertical direction.

The thermal insulation and flame resistance of c-MWCNT/ANF aerogel were visually confirmed by using an alcohol lamp as a heat source and placing some cotton on an asbestos wire gauze (Fig. 8e). Without the protection of the aerogel, the cotton quickly shrank and smoked at 30 s, whereafter turned into black at 60 s (Video S1). Nevertheless, the cotton remained intact after burning for 300 s when the aerogel isolated the heat source (Video S2). Moreover, the TGA curve also verifies the magnificent thermostability of the aerogel, with weight loss occurring at about 500 ℃ (Fig. 8f). The excellent thermostability ensures c-

MWCNT/ANF aerogels can work under high-temperature environments.

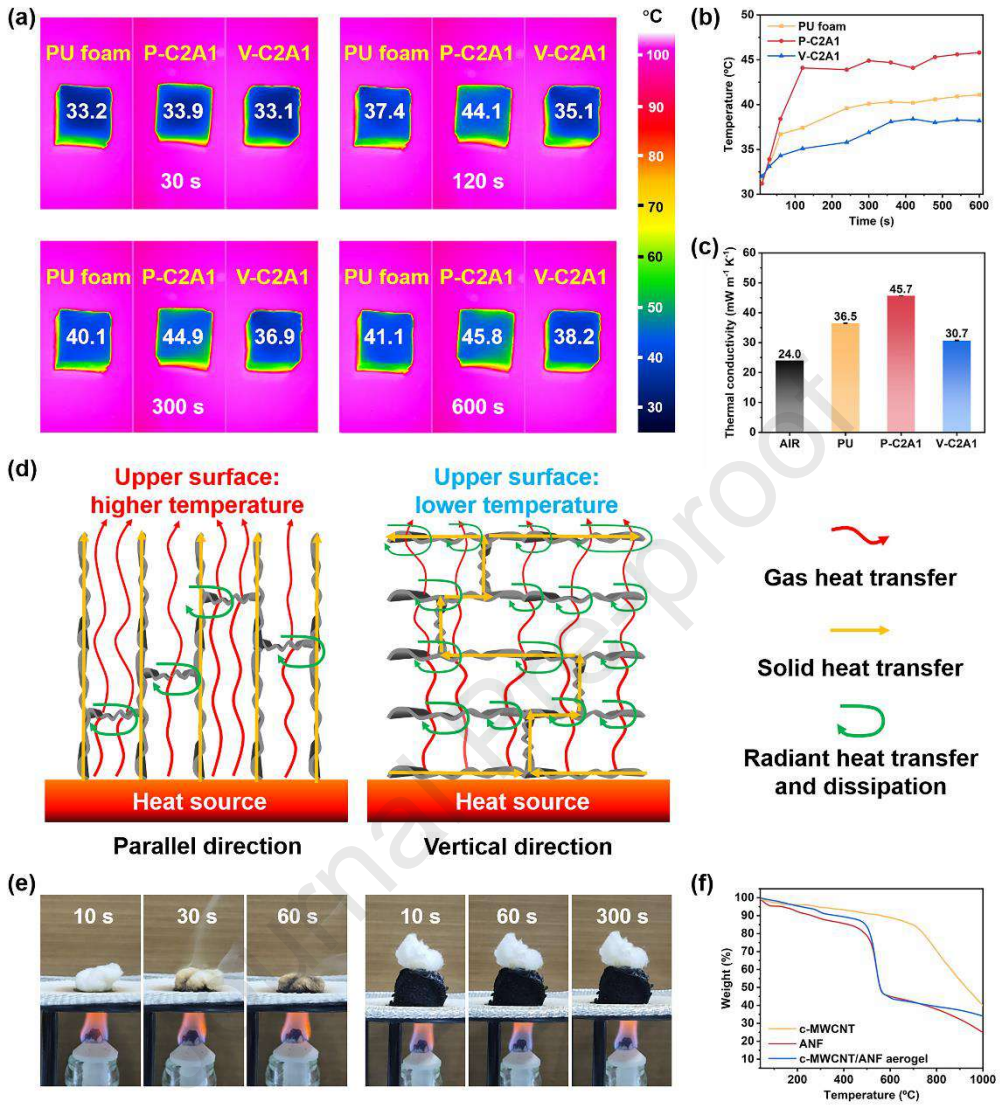

Fig. 8. (a) Thermal infrared images of PU foam, P-C2A1, and V-C2A1 composite aerogels on a hot stage of 100 °C for 600 s, and (b) corresponding temperature–time curves of the upper surface; (c) Thermal conductivities of PU foam, P-C2A1, and V-C2A1 composite aerogels; (d) The mechanism of heat transfer along the parallel and vertical directions of anisotropic aerogel. (e) Comparison of cotton heated by flame without and with c-MWCNT/ANF composite aerogels; (f) TGA curves of c-MWCNT powder, ANF, and c-MWCNT/ANF composite aerogel.

3.6 Mechanical property

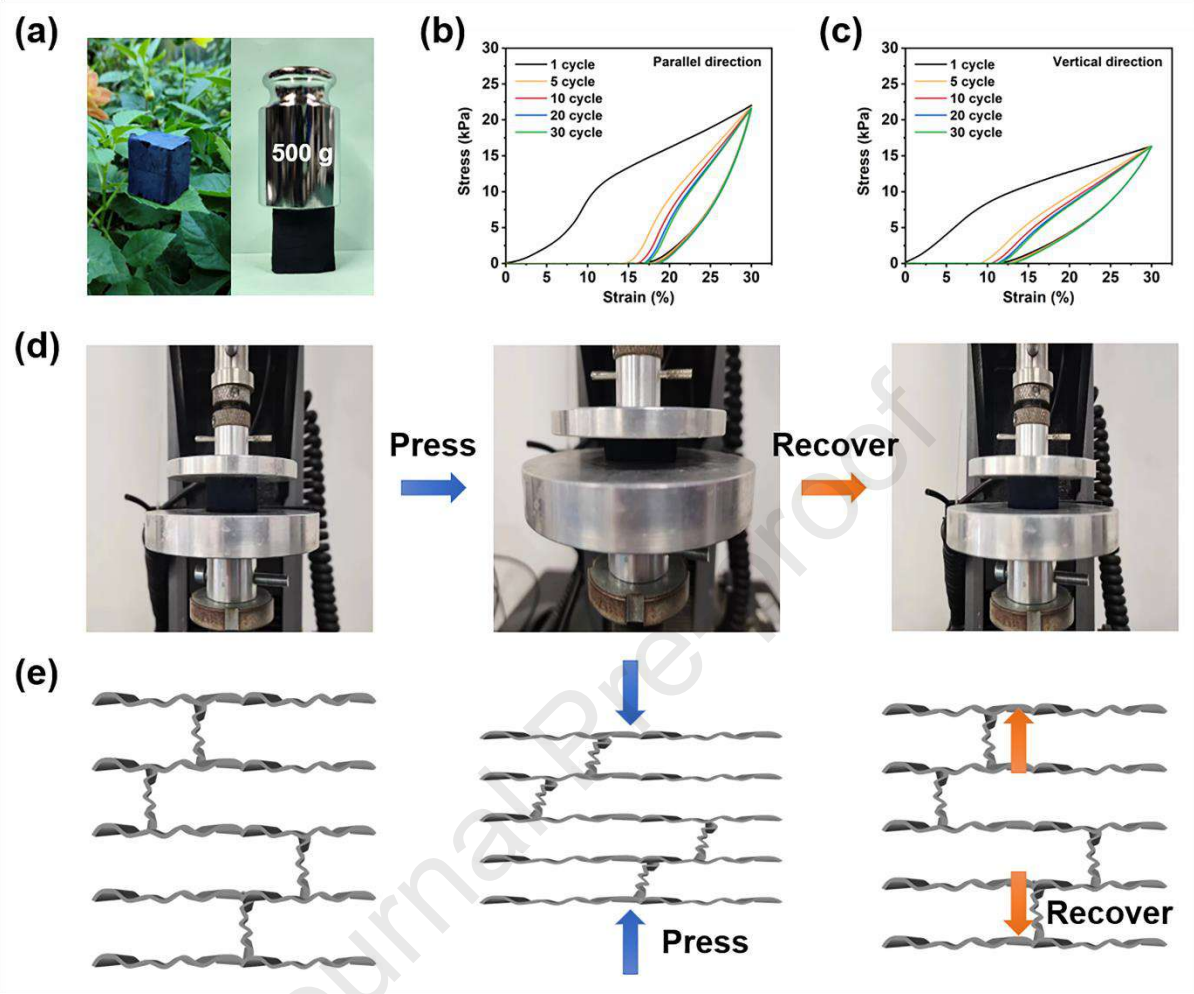

Fig. 9. (a) an aerogel standing on a leaf and supporting a 500 g weight along the parallel direction. Cyclic compressive stress−strain curves of the C2A1 aerogel along (b) parallel and (c) vertical directions. (d) Digital photo and (e) schematic diagram of C2A1 aerogel during compression and recovery along the vertical direction.

On the one hand, the formation of hydrogen bonds between c-MWCNT and ANF increases the adhesion between the two fillers and improves the strength of the aerogel skeleton. On the other hand, honeycomb-like structures endow c-MWCNT/ANF aerogels with

anisotropic mechanical strength along the parallel and vertical directions. When the force is applied along the parallel direction of the hole, the wall of the hole can support greater weight. As displayed in Fig. 9a, a C2A1 aerogel not only has a low density but also can support an object 1000 times its weight along the parallel direction. In addition, Fig. 9b and c depict the cyclic compressive stress−strain curves of the C2A1 aerogel at 30% strain for 30 cycles along the parallel and vertical directions, respectively. Along the parallel direction, the compression strength and recovery strain of C2A1 aerogel is about 22.0 kPa and 16.3% on the first compression cycle. After 30 compression cycles, the compression strength decreases to 21.6 kPa and the recovery strain increases to 18.3%. Along the vertical direction, the compression strength and recovery strain of C2A1 aerogel is about 16.4 kPa and 11.4% on the first compression cycle. After 30 compression cycles, the compression strength keeps 16.4 kPa and the recovery strain increases to 12.5%. By comparison, the parallel direction of C2A1 aerogel has a higher compression strength, but the vertical direction of C2A1 aerogel has a better recovery ability, proving that the mechanical properties of C2A1 aerogel closely depend on the honeycomb-like structure. Fig. 9d exhibits the process of compression and recovery of C2A1 aerogel along the vertical direction, and Fig. 9e diagrams the reversible bending deformation for the skeleton during the compression and recovery.

4. Conclusion

Based on the negative charge repulsion, protonation, and gelation of c-MWCNT/ANF under different solvent systems, c-MWCNT/ANF composite aerogels were successfully fabricated through unidirectional freezing and freeze-drying. The composite aerogels with

oriented channel structures exhibit anisotropic EMWA, electrical conductivity, compression, and thermal insulation properties in different directions. At a mass ratio of c-MWCNT to ANF of 2:1, the composite aerogel shows an RL_{min} of -60.43 dB and a maximum EAB of 5.34 GHz along the vertical direction. Additionally, with an initial decomposition temperature exceeding 500 °C, the composite aerogel demonstrates remarkable thermal stability and flame resistance. Moreover, owing to the high porosity (~ 98.4%), the composite aerogel exhibits ultralow density (~ 26.2 g cm^{-3}) and excellent thermal insulation. These characteristics indicate promising applications in EMWA and infrared stealth.

Acknowledgement

This work was financially supported by the National Key R&D Program of China (2022YFB3805700).

References

[1] A. Hazarika, B.K. Deka, K. Kong, D. Kim, Y.-W. Nam, J.-H. Choi, et al., Microwave absorption and mechanical performance of α-MnO2 nanostructures grown on woven Kevlar fiber/reduced graphene oxide-polyaniline nanofiber array-reinforced polyester resin composites, Composites Part B: Engineering 140 (2018) 123-132.

[2] Q. Li, Z. Zhang, L. Qi, Q. Liao, Z. Kang, Y. Zhang, Toward the Application of High Frequency Electromagnetic Wave Absorption by Carbon Nanostructures, Advanced Science 6(8) (2019) 1801057.

[3] F. Wu, P. Hu, F. Hu, Z. Tian, J. Tang, P. Zhang, et al., Multifunctional MXene/C Aerogels for Enhanced Microwave Absorption and Thermal Insulation, Nano-Micro Letters 15(1) (2023)

194.

[4] H. Lv, Z. Yang, H. Pan, R. Wu, Electromagnetic absorption materials: Current progress and new frontiers, Progress in Materials Science 127 (2022) 100946.

[5] J. Wang, J. Yang, J. Yang, Regulation mechanism for the formation and microwave absorbing performance of CNT/CoFe-MOF derived hierarchical composite, International Journal of Smart and Nano Materials 13(2) (2022) 273-292.

[6] L. Zhu, Y. Cao, B. Jiang, J. Yu, J. Zhu, Z. Hu, Compressible, elastic and 3D porous Ti3C2Tx MXene/RGO/CNCs composite aerogel for electromagnetic wave absorbing, Journal of Alloys and Compounds 969 (2023) 172117.

[7] D. Zhou, H. Yuan, Z. Yu, W. Guo, Y. Xiong, G. Luo, et al., Broadband electromagnetic absorbing performance by constructing alternate gradient structure (AGS) for PMMA-based foams, Composites Part A: Applied Science and Manufacturing 149 (2021) 106557.

[8] H. Qu, P. Zheng, T. Wang, X. Yu, J. Pan, X. Fan, et al., MOF-derived multi-interface carbon-based composites with enhanced polarization loss and efficient microwave absorption, International Journal of Smart and Nano Materials 13(3) (2022) 465-480.

[9] X. Zhao, D. Zhu, J. Wu, R. Zhang, X. Lu, B. Fan, et al., Environmentally friendly a multifunctional cellulose-based carbon foam for superior electromagnetic wave absorption performance, Composites Communications 35 (2022) 101320.

[10] Y. Shi, Z. Ma, X. Zhang, F. Yan, Y. Zhao, C. Zhu, et al., Flexible Film Constructed by Asymmetrically-Coordinated La1N4Cl1 Moieties on Interconnected Nitrogen-Doped Graphene Nanocages for High-Efficiency Electromagnetic Wave Absorption, Advanced

Functional Materials (2023) 2313483.

[11] L. Ni, S. Chen, X. Jiang, Y. Luo, H. Zou, P. Liu, Anisotropic electromagnetic wave absorption performance of Polyimide/multi-walled carbon nanotubes composite aerogels with aligned slit-like channels structure, Composites Part A: Applied Science and Manufacturing 154 (2022) 106781.

[12] L. Kong, S. Zhang, Y. Liu, H. Wu, X. Fan, Y. Cao, et al., Hierarchical architecture bioinspired CNTs/CNF electromagnetic wave absorbing materials, Carbon 207 (2023) 198-206.

[13] M. Cao, X. Wang, W. Cao, X. Fang, B. Wen, J. Yuan, Thermally Driven Transport and Relaxation Switching Self-Powered Electromagnetic Energy Conversion, Small 14(29) (2018) 1800987.

[14] Z. Sun, V. Nicolosi, D. Rickard, S.D. Bergin, D. Aherne, J.N. Coleman, Quantitative Evaluation of Surfactant-stabilized Single-walled Carbon Nanotubes: Dispersion Quality and Its Correlation with Zeta Potential, The Journal of Physical Chemistry C 112(29) (2008) 10692-10699.

[15] M.D. Vo, D.V. Papavassiliou, Physical adsorption of polyvinyl pyrrolidone on carbon nanotubes under shear studied with dissipative particle dynamics simulations, Carbon 100 (2016) 291-301.

[16] X.-X. Wang, M. Zhang, J.-C. Shu, B. Wen, W.-Q. Cao, M.-S. Cao, Thermally-tailoring dielectric “genes” in graphene-based heterostructure to manipulate electromagnetic response, Carbon 184 (2021) 136-145.

[17] J. Cai, C. Griesbach, R. Thevamaran, Extreme Dynamic Performance of Nanofiber Mats

under Supersonic Impacts Mediated by Interfacial Hydrogen Bonds, ACS Nano 15(12) (2021) 19945-19955.

[18] H. Zhang, N. Luo, T. Liu, F. Chen, Q. Fu, Light-weight, low-loading and large-sheet reduced graphene oxide for high-efficiency microwave absorber, Carbon 196 (2022) 1024-1034.

[19] Y. Ding, J. Zhu, S. Wang, M. Yang, S. Yang, L. Yang, et al., Dependence of reduction degree on electromagnetic absorption of graphene nanoribbon unzipped from carbon nanotube, Journal of Colloid and Interface Science 552 (2019) 196-203.

[20] Z. Zhao, B. Kang, J. Xu, C. Zhu, X. Zhang, X. Zhang, et al., N-doped carbon hollow spheres supported N-doped carbon nanotubes for efficient electromagnetic wave absorption, Carbon 209 (2023) 117995.

[21] Y. He, S. Li, L. Zhou, C. Wei, C. Yu, Y. Chen, et al., Cellulose nanofibrils-based hybrid foam generated from Pickering emulsion toward high-performance microwave absorption, Carbohydrate Polymers 255 (2021) 117333.

[22] J.Y. Oh, S.J. Yang, J.Y. Park, T. Kim, K. Lee, Y.S. Kim, et al., Easy Preparation of Self-Assembled High-Density Buckypaper with Enhanced Mechanical Properties, Nano Letters 15(1) (2015) 190-197.

[23] W.-b. Zhang, X.-l. Xu, J.-h. Yang, T. Huang, N. Zhang, Y. Wang, et al., High thermal conductivity of poly(vinylidene fluoride)/carbon nanotubes nanocomposites achieved by adding polyvinylpyrrolidone, Composites Science and Technology 106 (2015) 1-8.

[24] C. Liu, Z. Zeng, J. Qiao, Q. Wu, W. Liu, F. Gao, et al., Versatile cellulose nanofibril

assisted preparation of ultralight, scalable carbon nanotube aerogel-based electromagnetic wave absorbers with ultrahigh reflection loss, Carbon 213 (2023) 118277.

[25] M. Aghvami-Panah, A. Wang, M. Panahi-Sarmad, S.A.S. Esfahani, A.A. Seraji, M. Shahbazi, et al., A comparison study on polymeric nanocomposite foams with various carbon nanoparticles: adjusting radiation time and effect on electrical behavior and microcellular structure, International Journal of Smart and Nano Materials 13(3) (2022) 504-528.

[26] Z. Huang, R. Qin, H. Zhang, M. Guo, D. Zhang, C. Gao, et al., Ambient-drying to construct unidirectional cellulose nanofibers/ carbon nanotubes aerogel with ultra-lightweight, robust, and superior microwave absorption performance, Carbon 212 (2023) 118150.

[27] Y. Zhou, S.-j. Wang, D.-s. Li, L. Jiang, Lightweight and recoverable ANF/rGO/PI composite aerogels for broad and high-performance microwave absorption, Composites Part B: Engineering 213 (2021) 108701.

[28] J. Xu, M. Liu, X. Zhang, B. Li, X. Zhang, X. Zhang, et al., Atomically dispersed cobalt anchored on N-doped graphene aerogels for efficient electromagnetic wave absorption with an ultralow filler ratio, Applied Physics Reviews 9(1) (2022).

[29] J. Luo, Y. Wang, Z. Qu, W. Wang, D. Yu, Anisotropic, multifunctional and lightweight CNTs@CoFe2O4/polyimide aerogels for high efficient electromagnetic wave absorption and thermal insulation, Chemical Engineering Journal 442 (2022) 136388.

[30] X. Jia, J. Wang, X. Zhu, T. Wang, F. Yang, W. Dong, et al., Synthesis of lightweight and flexible composite aerogel of mesoporous iron oxide threaded by carbon nanotubes for microwave absorption, Journal of Alloys and Compounds 697 (2017) 138-146.

[31] M.C. Vu, H. Kang, P.J. Park, B.-G. Choi, J.-W. Paik, W.-K. Choi, et al., Scalable graphene fluoride sandwiched aramid nanofiber paper with superior high-temperature capacitive energy storage, Chemical Engineering Journal 444 (2022) 136504.

[32] X. Zhang, A. Wang, X. Zhou, F. Chen, Q. Fu, Fabrication of aramid nanofiber-wrapped graphene fibers by coaxial spinning, Carbon 165 (2020) 340-348.

[33] A. Wang, X. Zhang, F. Chen, Q. Fu, Aramid nanofiber framework supporting graphene nanoplate via wet-spinning for a high-performance filament, Carbon 179 (2021) 655-665.

[34] X.-X. Wang, Q. Zheng, Y.-J. Zheng, M.-S. Cao, Green EMI shielding: Dielectric/magnetic "genes" and design philosophy, Carbon 206 (2023) 124-141.

[35] M. Yang, K. Cao, L. Sui, Y. Qi, J. Zhu, A. Waas, et al., Dispersions of Aramid Nanofibers: A New Nanoscale Building Block, ACS Nano 5(9) (2011) 6945-6954.

[36] S. Chen, Z. Li, J. Huang, L. Sha, Z. Lu, Electrically conductive yet insulating aramid nanofiber Janus films via gel–gel assembling for flexible motion sensing and Joule heating, Chemical Engineering Journal 457 (2023) 141021.

[37] L. Yin, B. Zhang, M. Tian, N. Ning, L. Zhang, W. Wang, Surface construction of ANF/CNT onto aramid fibers to enhance interfacial adhesion and provide real-time monitoring of deformation, Composites Science and Technology 223 (2022) 109336.

[38] L. Li, X. Yuan, H. Zhai, Y. Zhang, L. Ma, Q. Wei, et al., Flexible and Ultrathin Graphene/Aramid Nanofiber Carbonizing Films with Nacre-like Structures for Heat-Conducting Electromagnetic Wave Shielding/Absorption, ACS Applied Materials & Interfaces 15(12) (2023) 15872-15883.

[39] J. Huang, J. Li, X. Xu, L. Hua, Z. Lu, In Situ Loading of Polypyrrole onto Aramid Nanofiber and Carbon Nanotube Aerogel Fibers as Physiology and Motion Sensors, ACS Nano 16(5) (2022) 8161-8171.

[40] J. Zhu, W. Cao, M. Yue, Y. Hou, J. Han, M. Yang, Strong and Stiff Aramid Nanofiber/Carbon Nanotube Nanocomposites, ACS Nano 9(3) (2015) 2489-2501.

[41] L. Liang, Q. Li, X. Yan, Y. Feng, Y. Wang, H.-B. Zhang, et al., Multifunctional Magnetic Ti3C2Tx MXene/Graphene Aerogel with Superior Electromagnetic Wave Absorption Performance, ACS Nano 15(4) (2021) 6622-6632.

[42] X. Su, J. Wang, M. Han, Y. Liu, B. Zhang, S. Huo, et al., Broadband electromagnetic wave absorption using pure carbon aerogel by synergistically modulating propagation path and carbonization degree, Journal of Colloid and Interface Science 652 (2023) 780-788.

[43] J. Cheng, L. Cai, Y. Shi, F. Pan, Y. Dong, X. Zhu, et al., Polarization loss-enhanced honeycomb-like MoS2 nanoflowers/undaria pinnatifida-derived porous carbon composites with high-efficient electromagnetic wave absorption, Chemical Engineering Journal 431 (2022) 134284.

[44] H. Cheng, Y. Pan, X. Wang, C. Liu, C. Shen, D.W. Schubert, et al., Ni Flower/MXene-Melamine Foam Derived 3D Magnetic/Conductive Networks for Ultra-Efficient Microwave Absorption and Infrared Stealth, Nano-Micro Letters 14(1) (2022) 63.

[45] W. He, J. Zheng, W. Dong, S. Jiang, G. Lou, L. Zhang, et al., Efficient electromagnetic wave absorption and Joule heating via ultra-light carbon composite aerogels derived from bimetal-organic frameworks, Chemical Engineering Journal 459 (2023) 141677.

[46] Y. Liu, X. Wei, X. He, J. Yao, R. Tan, P. Chen, et al., Multifunctional Shape Memory Composites for Joule Heating, Self-Healing, and Highly Efficient Microwave Absorption, Advanced Functional Materials 33(5) (2023) 2211352.

[47] C. Gao, H. Zhang, D. Zhang, F. Gao, Y. Liu, X. Chen, et al., Sustainable synthesis of tunable 2D porous carbon nanosheets toward remarkable electromagnetic wave absorption performance, Chemical Engineering Journal 476 (2023) 146912.

[48] Q. Zheng, J. Wang, M. Yu, W.-Q. Cao, H. Zhai, M.-S. Cao, Heterodimensional structure porous nanofibers embedded confining magnetic nanocrystals for electromagnetic functional material and device, Carbon 210 (2023) 118049.

[49] M.-S. Cao, W.-L. Song, Z.-L. Hou, B. Wen, J. Yuan, The effects of temperature and frequency on the dielectric properties, electromagnetic interference shielding and microwave-absorption of short carbon fiber/silica composites, Carbon 48(3) (2010) 788-796.

[50] F. Yang, J. Yao, Z. Shen, Q. Ma, G. Peng, J. Zhou, et al., Multifunctional carbon nanotubes-based hybrid aerogels with high-efficiency electromagnetic wave absorption at elevated temperature, Journal of Colloid and Interface Science 638 (2023) 843-854.

Highlights

- ANF ameliorates the dispersibility and electromagnetic parameters of c-MWCNT.
- Anisotropic and multifunctional c-MWCNT/ANF aerogel was prepared.
- The reflection loss and effective absorption bandwidth reach -60.43 dB and 5.34 GHz.
- The aerogel has ultralow density, thermal insulation, and flame resistance.

Declaration of interests

☒ The authors declare that they have no known competing financial interests or personal relationships that could have appeared to influence the work reported in this paper.

☐ The authors declare the following financial interests/personal relationships which may be considered as potential competing interests: